Monthly Notices
of the
ROYAL ASTRONOMICAL SOCIETY

MNRAS **464,** 3029–3039 (2017)
Advance Access publication 2016 September 5

doi:10.1093/mnras/stw2219

# A high-resolution H I study towards the supernova remnant Puppis A and its environments

E. M. Reynoso,[1]★ S. Cichowolski[1] and A. J. Walsh[2]

[1]*Instituto de Astronomía y Física del Espacio (IAFE), UBA-CONICET, Av. Int. Güiraldes 2620, Pabellón IAFE, Ciudad Universitaria, Ciudad Autónoma de Buenos Aires C1428ZAA, Argentina*
[2]*International Centre for Radio Astronomy Research, Curtin University, GPO Box U1987, Perth, WA 6845, Australia*

Accepted 2016 September 1. Received 2016 August 16; in original form 2016 May 5

## ABSTRACT

We observed the supernova remnant Puppis A in the 21 cm line with the Australia Telescope Compact Array with the aim of determining the systemic velocity and, hence, the corresponding kinematic distance. For the compact, background sources in the field, we obtain absorption spectra by applying two methods: (a) subtracting profiles on- and off-source towards continuum emission, and (b) filtering short spacial frequencies in the Fourier plane to remove large-scale emission. One of the brightest features to the east of the shell of Puppis A was found to be a background source, probably extragalactic. Removing the contribution from this and the previously known unrelated sources, the systemic velocity of Puppis A turns out to be limited between 8 and 12 km s$^{-1}$, which places this source at a distance of 1.3 $\pm$ 0.3 kpc. From the combined images that include both single-dish and interferometric data, we analyse the distribution of the interstellar hydrogen. We suggest that an ellipsoidal ring at $v \sim +8$ km s$^{-1}$ could be the relic of a bubble blown by the progenitor of Puppis A, provided the distance is $\lesssim 1.2$ kpc. The main consequences of the new systemic velocity and distance as compared with previous publications ($v = +16$ km s$^{-1}$ and $d = 2.2$ kpc) are the absence of a dense interacting cloud to the east to explain the morphology, and the decrease of the shell size and the neutron star velocity, which are now in better agreement with statistical values.

**Key words:** stars: massive – ISM: bubbles – ISM: individual objects: Puppis A – ISM: supernova remnants – radio lines: ISM.

## 1 INTRODUCTION

H I absorption studies towards the continuum background offered by supernova remnants (SNR) reveal the distribution of the interstellar medium (ISM) gas along the line of sight and, combined with Galactic rotation models, can set limits on the remnants' distance. Reliable distance estimates are important to determine intrinsic properties of an SNR such as size, age, explosion energy or expansion velocity. In addition, H I emission at velocities beyond an SNR's systemic velocity or away from the direction of the remnant also give information about the ISM distribution and Galactic structure. Therefore, H I observations help to construct a three-dimensional picture of the ambient medium where an SNR is evolving, as well as to identify foreground or background structures in the Galaxy.

The southern Galactic SNR Puppis A is an extended, distorted shell, ∼50 arcmin in diameter, estimated to be between 3700 (Winkler et al. 1988) and 5200 (Becker et al. 2012) yr old. It is one of the brightest SNRs in X-rays (e.g. Hwang, Petre & Flanagan 2008) and has recently been detected in $\gamma$-rays (Hewitt et al. 2012). A pulsating X-ray compact central object (CCO) inside Puppis A confirms that the progenitor was a high-mass star (Petre, Becker & Winkler 1996; Zavlin, Trümper & Pavlov 1999). Winkler & Petre (2007) showed that the CCO is moving away from the explosion centre inferred from optical filaments (Winkler et al. 1988). Reynoso et al. (2003) found an elongated minimum in the H I emission at +16 km s$^{-1}$ coincident with the path followed by the CCO.

Several suggestions of interaction between Puppis A and nearby clouds have been reported, although the picture is not completely clear yet. Dubner & Arnal (1988) observed Puppis A in the 21 cm line and in the CO ($J = 1$–0) 2.6 mm line and found a molecular cloud to the east of the SNR coincident with a flattening in the radio continuum shell. The authors interpret this coincidence as evidence of a molecular cloud–SNR interaction, and set the systemic velocity of the remnant to be around +16 km s$^{-1}$. A subsequent H I study using VLA observations (Reynoso et al. 1995) supports the same result based on morphological coincidences, and infers a distance of 2.2 kpc. However, indubitable tracers of interactions between SNR and external clouds, like molecular broadenings or OH masers at 1720 MHz, have never been observed. A high-resolution CO study (Paron et al. 2008) failed to detect any gas concentration

★E-mail: ereynoso@iafe.uba.ar

associated with an X-ray bright knot to the east of the shell, previously interpreted as coming from a shocked interstellar cloud (Hwang, Flanagan & Petre 2005).

Frail et al. (1996) reported single-dish observations at 1720 MHz towards Puppis A performed with the Parkes and Greenbank telescopes, with negative detections. Woermann, Gaylard & Otrupcek (2000) observed several pointings towards Puppis A and in the immediate vicinity using the 26-m antenna at the Hartebeesthoek Radio Observatory in South Africa in the four 18 cm lines of OH and concluded that the systemic velocity of the remnant is 7.6 km s$^{-1}$ rather than +14 km s$^{-1}$, as proposed based on H I (Reynoso et al. 1995) and CO (Dubner & Arnal 1988) observations. The authors drew attention on the fact that they did detect the 1720 MHz line in emission, albeit at ∼3 km s$^{-1}$, where the other three lines appear in absorption. This emission may be hinting at the presence of an anomalous OH cloud like those reported by Turner (1982), which are associated with giant clouds and are tracers of the spiral arms.

The neutral and molecular density distribution around Puppis A is necessary to model the $\gamma$-ray emission and explain its origin. Additionally, the hydrogen column density is a key parameter to interpret the X-ray emission. In all cases, it is essential to establish the SNR's systemic velocity. Although morphological arguments help to infer this velocity, the most reliable method is to analyse the H I absorption. We note that high-quality absorption studies towards Puppis A are lacking. The previous VLA H I study (Reynoso et al. 1995) has a poor velocity resolution (5.2 km s$^{-1}$) and several residual sidelobes make the identification of emission or absorption features rather unclear. The other absorption study conducted by Woermann et al. (2000) in OH lines has poor angular resolution (∼20 arcmin) and sampling (only 11 pointings on and off the SNR). In this paper, we analyse new high angular and spectral resolution data in the H I 21 cm line in a mosaic centred at Puppis A in order to shed light on its kinematic distance and on the gas density distribution into which the shock front is expanding.

## 2 OBSERVATIONS AND DATA REDUCTION

Puppis A was observed simultaneously in the H I 21 cm line, in the four OH 18 cm lines, and in radio-continuum with the Compact Array Broadband Backend (CABB) of the Australia Telescope Compact Array (ATCA) in two 13 h runs. The first run took place on 2012 May 20 using the array configuration EW352 (baselines varying from 31 to 352 m excluding the sixth antenna), and the second, on 2012 July 6 in the 750A configuration (baselines from 77 to 735 m). A thorough analysis of the continuum data was published in Reynoso & Walsh (2015). The primary flux and bandpass calibrator was PKS 1934−638, while PKS 0823−500 was used for phase calibration. Due to the large angular size of Puppis A, observations were made in mosaicking mode with 24 pointings in order to cover not only the SNR but also its surroundings. Following the Nyquist theorem, the pointings were separated by 19.6 arcmin to optimize the sampling at 1.4 GHz. The radio continuum was observed using a 2 GHz bandwidth divided into 2048 channels of 1 MHz width, centred at 1750 MHz. The CABB allowed us to observe simultaneously a fine resolution 1 MHz 'zoom' band composed of 2048 channels of 0.5-kHz width, which were centred on the H I line and on the four ground state OH lines, at 1612, 1665, 1667 and 1720 MHz.

The data reduction was carried out with the MIRIAD software package (Sault, Teuben & Wright 1995). The first run observations (configuration EW352) were affected by a bug that was fixed before the second run took place: the CABB only read the first eight characters of a mosaic field name, and as a result, fields 10–19 were set to the phase centre of field 1, and fields 20–24, to that of field 2. To overcome this problem, we have split the uv data for the different fields, set the correct phase centre for each field in its header, and shifted the data to the new phase centre using the MIRIAD task UVEDIT. Having performed these steps, we followed henceforth a joint deconvolution. This correction was not necessary for the second run observations (configuration 750A).

Apart from the long mosaic name length bug, there was an additional CABB bug that affected the observations made in the 1 MHz zoom mode: the first correlator cycle was corrupted in such a way that the emission was shifted in frequency. To fix this problem, all first cycles had to be discarded. However, since off-source cycles are discarded by default when loading the data into MIRIAD, in principle it is not possible to determine when the first cycle in a scan is the first correlator cycle. Thus, we loaded the data with the 'unflag' option so as to keep all data, even the flagged ones, and then flagged every first cycle using the MIRIAD task QVACK. This procedure was applied for data from both May and July observe runs.

The remaining data reduction was standard. To improve the signal-to-noise ratio and save disc space at the same time, the data were Hanning smoothed as they were loaded into MIRIAD, and only every second channel was kept, amounting to a total of 1536 channels of 1 kHz width. After amplitude, bandpass and gain calibration, the continuum component was removed from the uv-data subtracting a linear fit to 550 line-free channels. An H I cube was constructed merging the data obtained with both ATCA configurations. Uniform weighting was applied.

The noise level was reduced at the expense of reducing the spectral resolution: we collapsed each four channels into one so as to increase the number of visibilities per channel by a factor of 4, and kept only one in every four channels. As a result, the H I cube has 213 channels spanning from −23 to 151.81 km s$^{-1}$, with an increment of 0.82 km s$^{-1}$. Although MOSMEM is a more robust task to clean a mosaic, it only copes with positive flux density values. Since H I absorption data are negative, we performed the cleaning with the MIRIAD task MOSSDI which, although optimized for point sources, can deal with negative components. After a deep cleaning, most sidelobes were removed. The noise achieved varies between approximately 2 and 9 mJy beam$^{-1}$. The noise is lower for channels with lower H I emission. Besides, regions that are covered by more than one mosaic field have a lower noise, which means that the noise increases towards the edges of the map. The images were restored with a beam of 118.3 × 88.9 arcsec, with a position angle of −4.°3.

To recover structures with the shortest spatial frequencies, the ATCA data were combined in the uv plane with single-dish data from the 64-m Parkes telescope, which are part of the Galactic All-Sky Survey (GASS, McClure-Griffiths et al. 2009). This step was performed with the MIRIAD task IMMERGE. No tapering was applied to the low-resolution cube. All pixels falling outside the mosaic were blanked out.

As an alternative way to produce absorption profiles, we have also followed the method proposed by Dickey et al. (2003): we constructed a higher resolution cube by filtering out all spatial frequencies lower than 168 m (0.8 kλ). We have not subtracted any continuum baseline this time, and the line free channels were used later to form an ancillary radio continuum image. After cleaning the H I cube with the MIRIAD task MOSSDI, a noise level of $\gtrsim$ 30 mJy beam$^{-1}$ was achieved. The beam is 69.4 × 45.6 arcsec, with a position angle of −1.°9. The way in which this cube will be used to obtain absorption spectra will be explained in detail in Section 3.1.

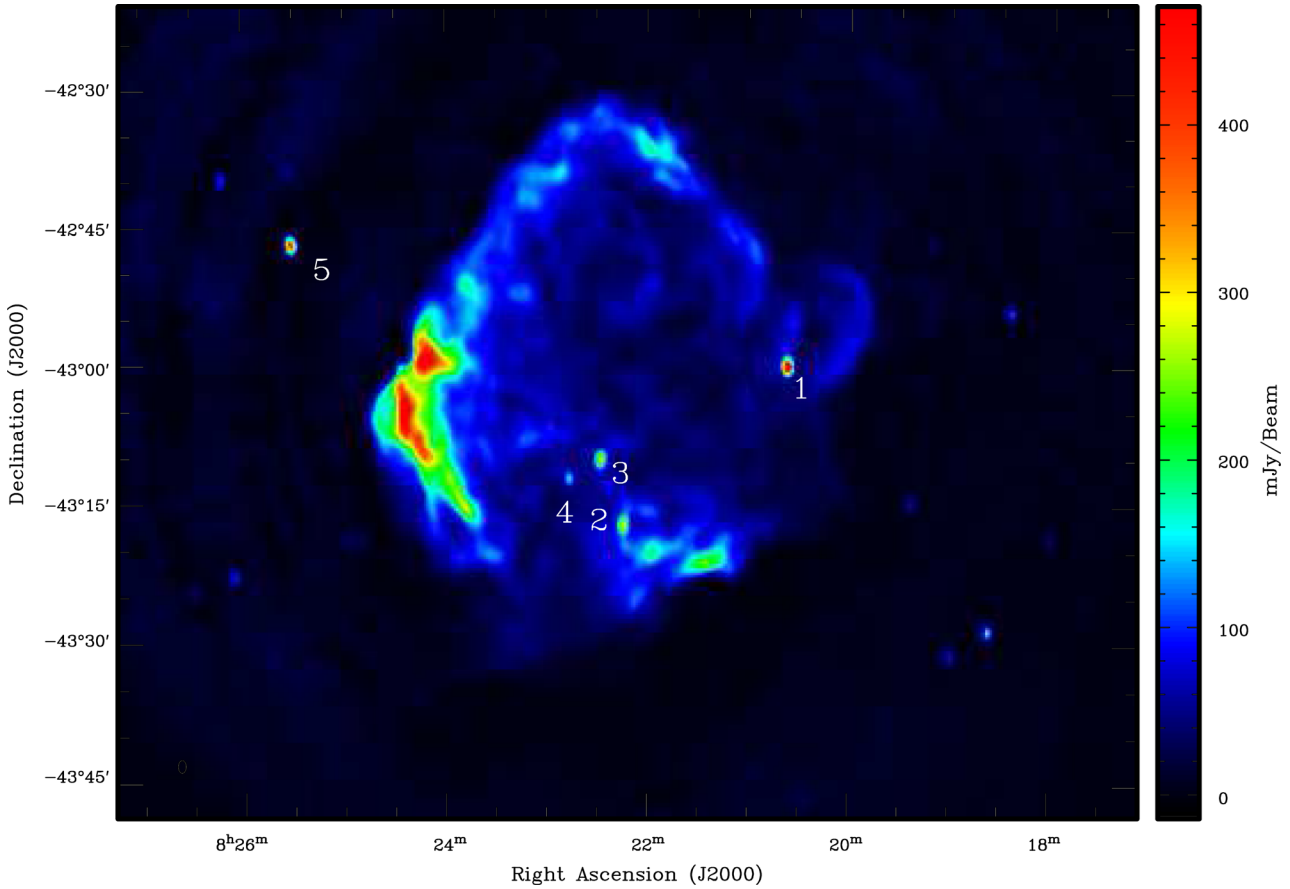


**Figure 1.** A continuum image of Puppis A at 1.4 GHz reproduced from Reynoso & Walsh (2015). The beam size is 82.2 × 50.6 arcsec, with a position angle of −0.°55, and is plotted at the bottom-left corner. The flux density scale is shown at the right. The noise level is 1.5 mJy beam$^{-1}$. The white numbers 1–5 on selected compact sources correspond to the labelling applied in Reynoso & Walsh (2015).

## 3 RESULTS

### 3.1 Absorption profiles

Puppis A is an extended radio source, with a diameter of almost 1°. Therefore, the density distribution of the ISM is not expected to be uniform across its face. In order to avoid misinterpretations of absorption profiles towards Puppis A that could arise in local inhomogeneities, we will make use of the strong compact sources 1–5 (Fig. 1) to compare their profiles with Puppis A and attempt set a reliable limit in the systemic velocity of the SNR.

The equation of radiative transfer states that the emission $T_{b_v}$ at a velocity $v$ measured by a radio telescope is

$$T_{b_v} = T_s(1 - e^{-\tau_v}) + T_c\, e^{-\tau_v}, \quad (1)$$

where $T_s$ and $\tau_v$ are the spin temperature and the optical depth of the column of H I gas, and $T_c$ is the background continuum emission. The continuum emission was subtracted from the line data as described in Section 2, hence equation (1) becomes

$$T_{L_v} = T_{b_v} - T_c = (T_s - T_c)(1 - e^{-\tau_v}). \quad (2)$$

To construct absorption profiles, we need to infer what the profile would be if the continuum source were not present. This profile, usually called $T_{off}$, must be subtracted from the profile measured on the continuum source ($T_{on}$). According to equation (2), the difference $T_{on} - T_{off}$ yields

$$T_{on} - T_{off} = -T_c\,(1 - e^{-\tau_v}) \quad (3)$$

or equivalently,

$$e^{-\tau_v} = \frac{T_{on} - T_{off} + T_c}{T_c}. \quad (4)$$

The method we applied to estimate $T_{off}$ is as follows: we extracted a box surrounding each compact source allowing for a large enough area around it as to include a statistically significant number of pixels free of continuum emission. The continuum image was used as a template, and all those pixels with flux densities above a cutoff level low enough as to exclude any continuum emission from the compact source ($T_{cut_1}$) were blanked in each H I channel. The remaining pixels were used to fit a bilinear function to the box in each channel, and this fit was employed to fill in the blanked areas. With this procedure, the pixels of the H I cube above a cutoff continuum level in the template ($T_{cut_2}$) yield the on-source profile when the original values are used and the expected off-source profile when these are replaced by the bilinear fit. The error of the interpolation is given by the rms of the residuals between the bilinear approximation and the original values for the pixels used to perform the fit.

The emission–absorption spectrum pairs for the five compact sources indicated in Fig. 1 are plotted in Fig. 2. For each, the upper frame is the expected profile (black solid line) with the error envelope, computed as described above, in green. The lower frame displays the absorption profile (blue solid lines) estimated using equation (4), with the corresponding error envelope in blue dashed lines.

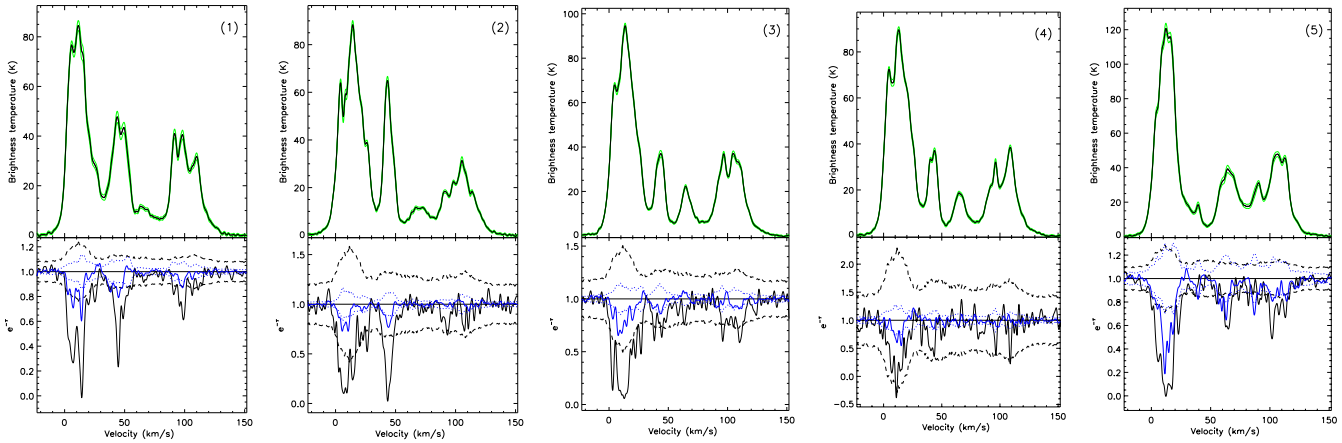


**Figure 2.** Emission–absorption spectrum pairs for the five compact sources shown in Fig. 1. The source number is shown at the top-right corner of each frame. The expected profiles are shown at the top, with the error envelopes in green. At the bottom, absorption profiles computed with two different methods are displayed: through the subtraction $T_{\rm on} - T_{\rm off}$ (blue solid lines), and through a short wavelength uv-filtering weighted by the radio continuum (black solid lines), as explained in the text. The error envelopes corresponding to each method are shown as dotted (first method) and dashed (second method) lines following the same colour code. In all cases, a Hanning smoothing was applied.

**Table 1.** Parameters of compact sources.

| Source number | RA (J2000) (h m s) | Dec. (J2000) (° ′ ″) | Spectral index[a] | Spectral index[b] | Cutoff levels for unfiltered radio continuum template[c] $T_{\rm cut_1}$ (K) | $T_{\rm cut_2}$ (K) | Cutoff level for uv-filtered radio continuum template[d] $T_{\rm cut}$ (K) | Peak radio continuum brightness temperature (K) |
|---|---|---|---|---|---|---|---|---|
| 1 | 08 20 35.6 | −43 00 23 | $-0.76 \pm 0.04$ | $-0.86 \pm 0.04$ | 10.8 | 23.2 | 29.2 | 106.3 |
| 2 | 08 22 13.4 | −43 17 38 | $-0.91 \pm 0.07$ | $-1.09 \pm 0.05$ | 17.8 | 20.9 | 17.4 | 43.5 |
| 3 | 08 22 27.0 | −43 10 29 | $-0.26 \pm 0.07$ | $-0.56 \pm 0.5$ | 10.8 | 12.4 | 16.6 | 47.3 |
| 4 | 08 22 45.7 | −43 12 38 | $-0.75 \pm 0.15$ | $-0.94 \pm 0.08$ | 8.8 | 12.2 | 8.5 | 24.6 |
| 5 | 08 25 30.7 | −42 46 57 | $-0.92 \pm 0.04$ | $-1.09 \pm 0.09$ | 0.8 | 3.1 | 21.0 | 84.2 |

[a]Index based on T-T plot (Reynoso & Walsh 2015).
[b]Index based on slope of $S(\nu)$ versus $\nu$ (Reynoso & Walsh 2015).
[c]Pixels above $T_{\rm cut_1}$ were replaced by bilinear interpolation, and pixels above $T_{\rm cut_2}$ were averaged to compute the absorption profile.
[d]Pixels above $T_{\rm cut}$ were averaged to compute the absorption profile.

For extended areas, the bilinear approximation is less accurate since the gaps between valid data to compute the fit are too large and a linear interpolation may not represent the missing points. An alternative way to estimate absorption profiles is to filter out extended emission in the Fourier domain. As mentioned in Section 2, we have constructed an H I cube without subtracting the continuum level and using only visibilities above 0.8 kλ, so that features with sizes larger than ∼4.5 arcmin are filtered out. Hence, the term involving $T_{\rm s}$ in equation (1) can be neglected and the remaining terms can be re-written as $e^{-\tau_v} = T_{\rm b_v}/T_{\rm c}$. To enhance absorption features in the profiles, we further weighted each pixel, $T_{\rm b_v}$, in the filtered H I cube by the corresponding radio continuum flux. To estimate the errors, for each channel we computed the rms on selected boxes towards three different regions away from radio continuum sources and obtained their averages. The profiles obtained by this method are plotted in black solid lines, with the $3\sigma$-error envelopes as black dashed lines.

In Table 1, we list the relevant parameters for the five compact sources and the determination of their absorption profiles. The first three columns contain their labels and coordinates. In the next two columns, we reproduce the spectral indices as measured in Reynoso & Walsh (2015) following two methods: T-T plots (fourth column) and a linear fit to the logarithmic plot $S_\nu$ versus $\nu$ (fifth column). The sixth column lists the cutoff brightness temperature of the radio continuum template map above which pixels in the H I cube were blanked and replaced by the bilinear fit computed with the remaining valid pixels within a box around each source. The seventh column displays the cutoff brightness temperature of the radio continuum template map above which the corresponding pixels in the H I cube were averaged to construct the $T_{\rm on}$ and $T_{\rm off}$ profiles. The eighth column indicates the cutoff brightness temperature of the uv-filtered radio continuum template map; the corresponding pixels above this value in the uv-filtered H I cube were used to construct a weighted absorption profile. The last column lists the peak radio continuum brightness temperature in the uv-filtered image, and is added with the intention of understanding the difference in the quality of the absorption profile of each source in terms of the difference in their intensities.

It is clear that the uv-filtering method produces spectra with deeper, more discernible absorption features. Besides, we note that the two methods give a closer result for source 5, which is the only one that is not projected behind Puppis A. The reason could be that since the rest of the sources are confused with the diffuse emission from the remnant, it is not easy to obtain an H I profile $T_{\rm on}$. Therefore, we will apply the uv-filtering method to measure the absorption on Puppis A, since it proves to be the most convenient tool for that purpose.

To isolate the contribution from Puppis A only in the uv-filtered cube, we blanked four boxes around sources 1–4. A first spectrum showed several absorption features up to $v \gtrsim +100$ km s$^{-1}$,

implying that additional extragalactic sources were contaminating the emission from Puppis A. Thus, we constructed profiles over selected regions all over the remnant. An intrinsic problem of the uv-filtering method is that only the smallest features survive, and the fewer visibilities used translates in a poorer imaging and a higher noise. Therefore, a limited number of relevant regions are used for the absorption analysis. In the map presented in the top frame of Fig. 3, we show the region where the most significant results are obtained. We constructed an absorption spectrum towards the area enclosed by the green contour at 60 mJy beam$^{-1}$ within the inner rectangular box. The resulting spectrum, shown at the bottom, shows several absorption features at different velocities up to the outer Galactic limits. Most features are beyond the error band, indicating that the continuum emission arises in a background source, probably of extragalactic origin. This is in agreement with the result reported by Reynoso & Walsh (2015), who found that this feature (box 3 in their fig. 7) has a steep spectrum, $\alpha = -0.8 \pm 0.4$.

To get more insight into this finding, we built a radio continuum image at 2.4 GHz, filtering all visibilities below 3 k$\lambda$ to minimize the contribution from the extended emission associated with Puppis A. The image is shown in Fig. 4. A few contours in blue from the continuum unfiltered image presented in Fig. 1 are plotted to facilitate the location of the newly discovered features within Puppis A. The compact source 5 appears near the top-left corner of the map. The bright compact source located at the outermost contour of the shell, at RA(2000) = $8^{h}24^{m}27^{s}$, Dec.(2000) = $-43^{\circ}00'24''$ was reported in Reynoso & Walsh (2015) under number 27, as well as the two weak sources 30 and 33, both several minutes away from Puppis A, at a declination of $\sim -43^{\circ}10'$. It was not possible to determine the spectral index for any of these sources. In all radio continuum images of Puppis A, the brightest features are the extragalactic compact source 1 and the eastern filament at RA(2000) $\sim 8^{h}24^{m}25^{s}$. Our uv-filtered map suggests that the eastern filament is actually an elongated extragalactic source, roughly 2 min long, which we will label G260.72-3.16. Other point-like compact sources are observed within an $\sim$5 min radius around it.

Given that the bright eastern filament is a background source, we blanked this area and obtained a new spectrum towards the whole remnant. A correction based on the line free channels was applied to account for the continuum baseline not subtracted in the uv plane. The result is depicted in Fig. 5. In this profile, we observe clear absorption up to +10 km s$^{-1}$ but not beyond. In the next subsection, we will analyse the H I emission around this velocity to set a more stringent limit to the systemic velocity.

### 3.2 H I emission distribution

In this section, we inspect the H I data cube looking for signatures of the interaction between the SNR and the ISM. On the other hand, bearing in mind that the supernova (SN) progenitor was a high-mass star (Petre et al. 1996), we also look for any evidence of a pre-existing structure.

Fig. 6 shows the H I emission distribution in the area of Puppis A in the velocity range from +2.56 to +29.77 km s$^{-1}$. Each box shows the averaged emission in three consecutive channel images, giving an effective velocity resolution of 2.48 km s$^{-1}$. The central velocity of each image is shown in the upper-left corner of each box. For the sake of presentation, a value corresponding to the averaged brightness temperature at each radial velocity was first subtracted. The subtracted value is indicated at the top-right corner of each frame.

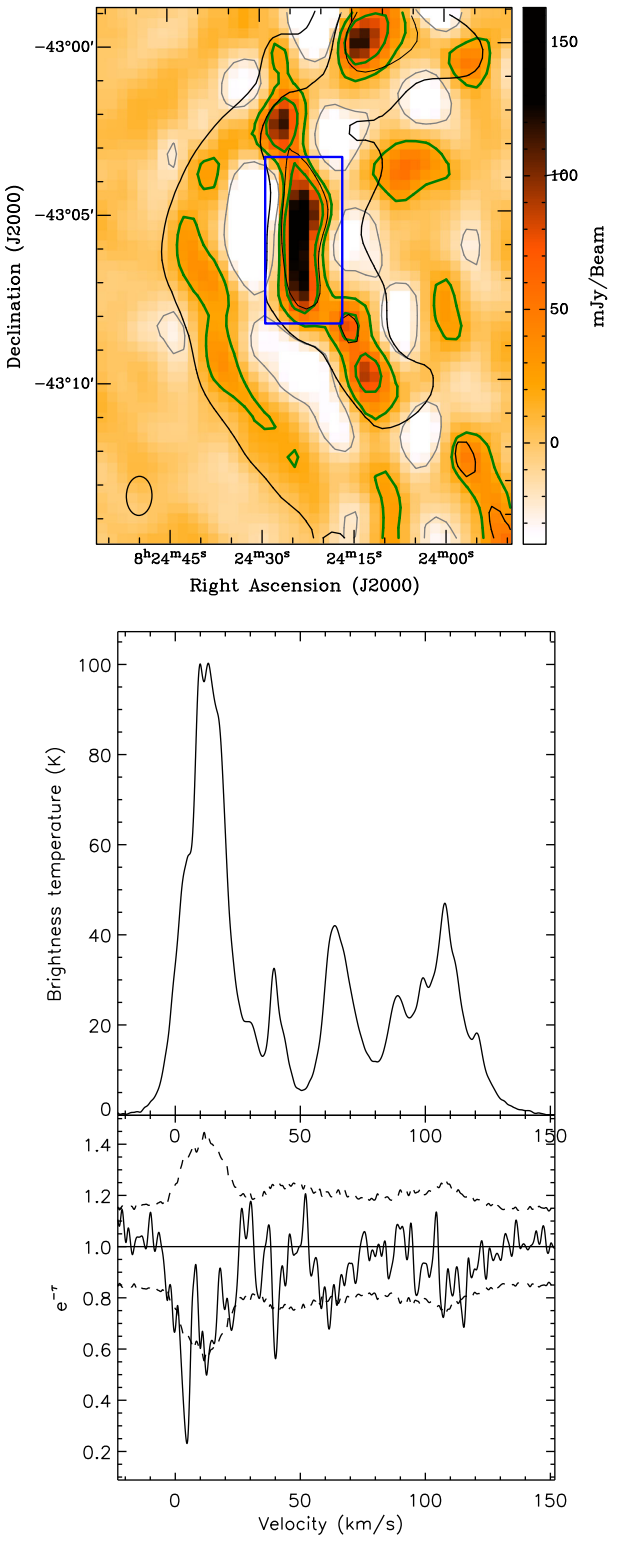


**Figure 3.** Top: radio continuum image of the eastern region of Puppis A as obtained from the line-free channels of the uv-filtered cube at 1420 MHz. Thick green contours at 20 and 60 mJy beam$^{-1}$ and thin grey contours at −20 mJy beam$^{-1}$ are overlaid. The beam is shown at the bottom-left corner. To facilitate the description, a few black contours from the unfiltered continuum image at 1.4 GHz are also plotted. Bottom: emission–absorption spectrum pair towards the region of Puppis A enclosed by the green contour at 60 mJy beam$^{-1}$ within the inner blue box (top panel). The 3$\sigma$-error envelope is plotted with a dashed line. A Hanning smoothing was applied.

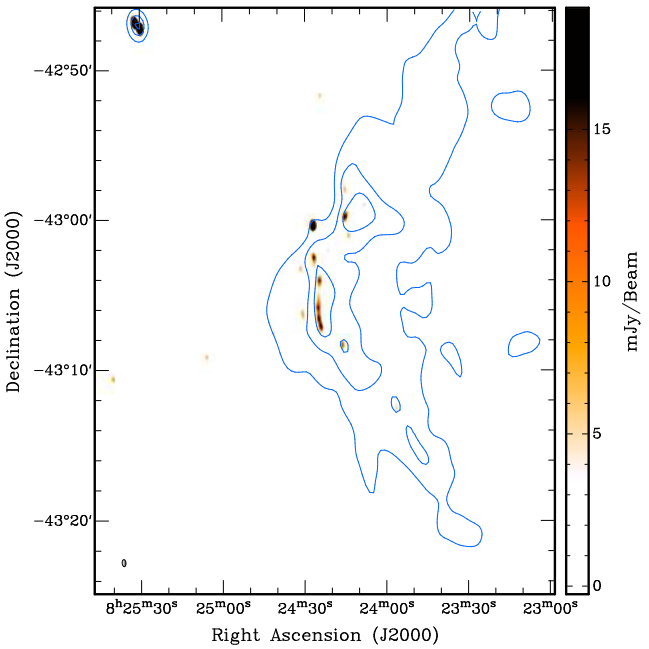


**Figure 4.** Image of the eastern region of Puppis A at 2.4 GHz filtered in the Fourier domain between 3 and 7 kλ. The beam is 28.1 × 15.2 arcsec, with a position angle of 4.°7, and is plotted at the bottom-left corner. The flux density scale is shown at the right. The noise level is 2 mJy beam$^{-1}$. To facilitate the comparison with the shell, a few blue contours from the unfiltered continuum image at 1.4 GHz are overlaid.

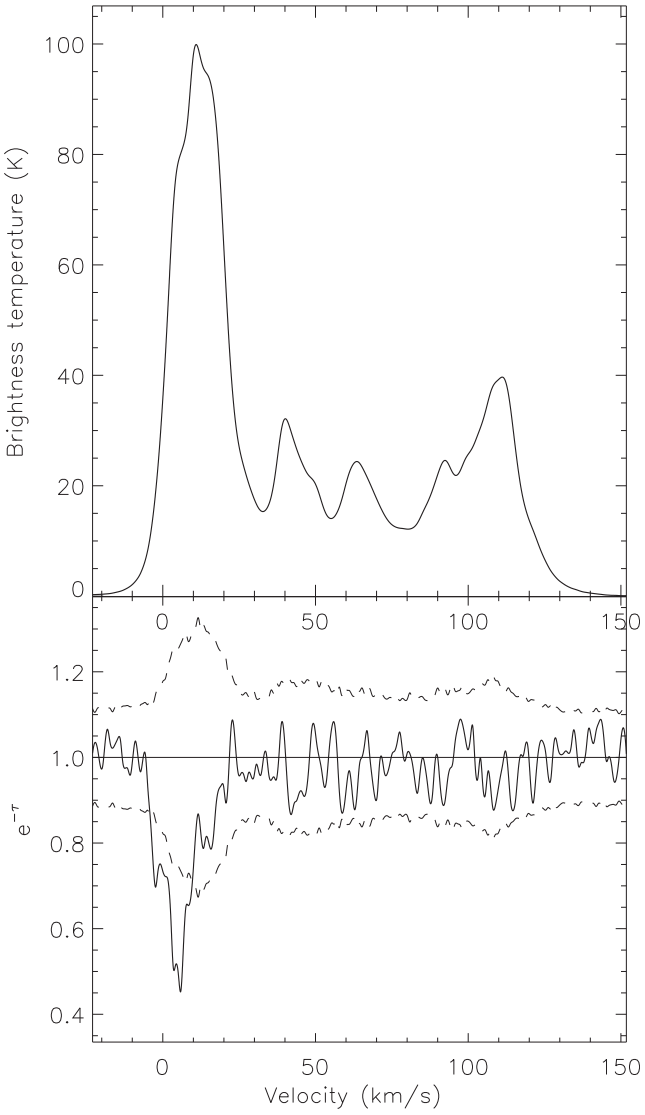


**Figure 5.** Emission–absorption spectrum pair of Puppis A. The compact sources 1–4 and the eastern bar have been removed. The 3$\sigma$-error envelope is plotted with a dashed line. Hanning smoothing was applied.

An inspection of Fig. 6 clearly shows that the brightest regions of the SNR are seen in absorption in the H I emission distribution at +2.56, +5.04, and +7.51 km s$^{-1}$. At $v$ = +12.46 km s$^{-1}$, a tight correlation between the northern edge of the shell and the outer contour of an H I concentration, could be revealing an interaction between the SNR shock front and the ISM at this velocity. At the same position but at a velocity of +7.51 km s$^{-1}$, a striking feature is observed. A close-up view of this region integrated between +5.86 and +8.34 km s$^{-1}$ is shown in Fig. 7, where the excellent spatial correlation observed suggests a link between this H I filament and Puppis A. From Fig. 6 it can be said that no obvious H I emission seems to be related to the SNR at velocities higher than $v$ = +12.46 km s$^{-1}$.

On the other hand, since the progenitor star of Puppis A was suggested to have a stellar mass between 15 and 25 M$_\odot$ (Hwang et al. 2008), as mentioned before, we look for an H I structure possibly created by such a star. It is well known that during their main-sequence phase, O-type stars create, through their high rate of energetic photons and strong stellar winds, interstellar bubbles (Weaver et al. 1977). These structures are detected in the H I emission distribution as areas of low emissivity surrounded, completely or partially, by expanding shells. A structure of this kind is observed at around +7.5 and +10 km s$^{-1}$ (see Fig. 6). Fig. 8 shows an image of the H I emission averaged between +6.69 and +9.98 km s$^{-1}$, where a shell-like structure is clearly observed at the location indicated by the ellipse. The structure seems to be open towards higher Galactic latitudes, probably as a consequence of the lower density found at this distance from the Galactic plane. The possible relation between this shell-like structure and the progenitor of Puppis A will be analysed in detail in Section 4.2.

## 4 DISCUSSION

As can be seen in Fig. 6, the H I distribution is far from uniform over Puppis A. This is also reflected in the difference observed in the profiles towards the compact sources 1 to 5. From Fig. 2, sources 1, 3, and 5 are clearly extragalactic since all of them show absorption features up to $v\sim+115$ km s$^{-1}$. Surprisingly, according to the spectral index, only source 5 could have been unmistakably asserted as extragalactic. Source 2 also has a spectral index typical of extragalactic sources, however the last absorption feature lies at only $v = \sim+45$ km s$^{-1}$. It is likely that absorption features at very high velocities (around +100 km s$^{-1}$) are masked by an overestimated error band, or the H I emission at such velocities in this direction is not strong enough to produce observable absorption. Finally, source 4, the weakest one (see last column in Table 1), does not show obvious absorption at velocities higher than $\sim+$ 10 km s$^{-1}$. The reason could be addressed either with the large error band or with a local origin for this source, which could even be associated with Puppis A, as suggested by Reynoso & Walsh (2015). Neither

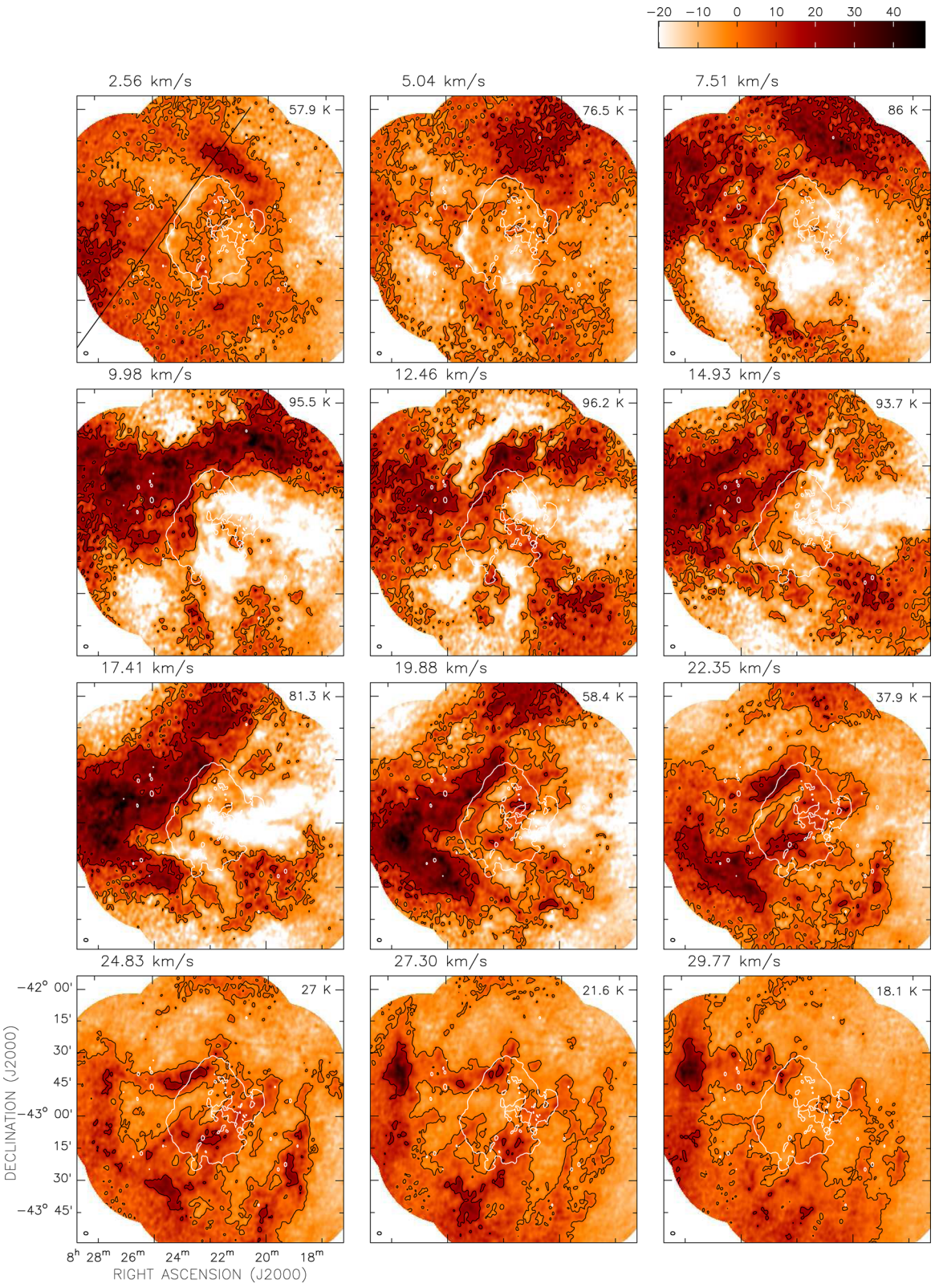


**Figure 6.** H I emission distribution between +2.56 and +29.77 km s$^{-1}$. The central velocity of each panel is given in the upper left-hand corner. Black contours are at 0 and 15 K. The white contour corresponds to the 0.03 mJy beam$^{-1}$ level of the radio continuum emission. The tilted line plotted superimposed on the emission at +2.56 km s$^{-1}$ indicates the line of Galactic latitude $b = -3°$. To use a same colour scale, an average brightness temperature, indicated at the top-right corner inside each frame, was subtracted from every channel. The colour scale, in K, is shown on top of the figure.

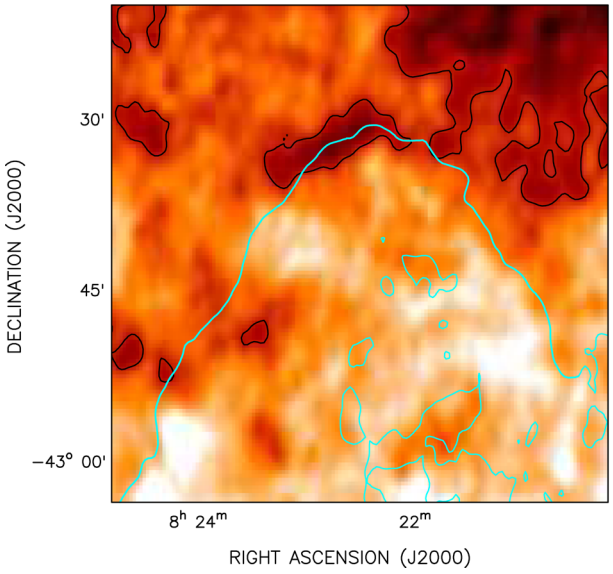


**Figure 7.** H I emission distribution averaged between +5.86 and +7.51 km s$^{-1}$. The black contour indicates the 94 K emission level, while the cyan contour corresponds to the 0.03 mJy beam$^{-1}$ level of the radio continuum emission.

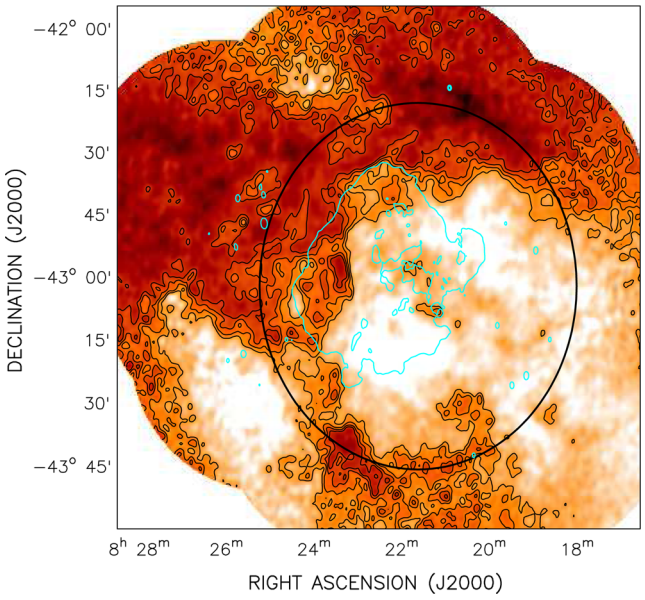


**Figure 8.** H I emission distribution averaged between +6.69 and +9.98 km s$^{-1}$. Black contours are from 85 to 100 K with a step of 5 K. The cyan contour corresponds to the 0.03 mJy beam$^{-1}$ level of the radio continuum emission. The ellipse shows the outline of the suggested H I bubble.

the absorption profile nor the spectral index enables us to derive a conclusive explanation about its origin.

While we have shown in Fig. 5 that Puppis A shows absorption only up to $v\sim +10$ km s$^{-1}$, the bright eastern background source projected on the shell (labelled G260.72-3.16 in this paper) shows absorption at $v\sim +40$, +60, and +115 km s$^{-1}$, and marginally at $v\sim +12.5$, +22.5, and +105 km s$^{-1}$ (Fig. 3). We note that, except for source 4, all other extragalactic sources show clear absorption around $v = +12$ km s$^{-1}$, with a confidence much better than $3\sigma$. The absence of an analogous feature in the absorption profile towards the whole remnant, even though the emission peak at this velocity is comparable to that at +8 and +10 km s$^{-1}$, implies that $v\sim +12$ km s$^{-1}$ can be reasonably set as an upper limit to the systemic velocity of Puppis A. The tight correlation between the northern edge of the shell and the H I at $v = +12.46$ km s$^{-1}$ mentioned in Section 3.2 could be revealing an interaction between the SNR shock front and the ISM at this velocity. Considering this possibility, we will adopt a conservative estimate of the systemic velocity of $v = +10.0 \pm 2.5$ km s$^{-1}$. This range encloses also the bubble found at $v\sim +8$ km s$^{-1}$ mentioned in Section 3.2, which will be analysed later. In this scenario, the H I filament at the northern edge of the shell (Fig. 7) might correspond to material pushed forward and compressed by the shock front.

### 4.1 Consequences of the new systemic velocity

Previous H I and molecular studies (Dubner & Arnal 1988; Reynoso et al. 1995, 2003) suggested a systemic velocity of around +16 km s$^{-1}$ for Puppis A. At this velocity, we observe an intensity gradient towards the Galactic plane, whose tilt is indicated through the $b = -3^\circ$ line (left upper box in Fig. 6). Hence, it appears that the H I emission here represents the gas density distribution of the Galactic plane. Our new data show that at $v = +16$ km s$^{-1}$, a good spatial correlation, although not in detail, is apparent *only* for the eastern border of the SNR, which runs parallel to the Galactic plane. A similar morphological match also appears up to $\sim +20$ km s$^{-1}$. However, there is no evidence to help disentangle whether this apparent correlation is due to a physical interaction between Puppis A and the ISM or just a projection effect.

In the light of the new absorption results, it is clear that the lower limit for the systemic velocity of Puppis A is $\sim +10$ km s$^{-1}$. As discussed above, a comparison with absorption spectra towards other field sources seems to set an upper limit at $v\sim +12.5$ km s$^{-1}$. Hence, although the +16 km s$^{-1}$ systemic velocity cannot be ruled out, we will follow the hypothesis of the alternative velocity $v = +10 \pm 2.5$ km s$^{-1}$.

The new systemic velocity proposed in this paper has implications in the explanation of the morphology of Puppis A. Between $v = +7.51$ and +12.46 km s$^{-1}$ (Fig. 6), there are no traces of any thick wall of material capable of explaining the flattened eastern edge of the SNR shell. The reason for such a morphology should be sought elsewhere, like the local ISM magnetic field. In this regard, we recall that the flattening is parallel to the Galactic plane (Fig. 6), and Reynoso, Hughes & Moffett (2013) have shown that in the case of SN 1006 the ISM magnetic field is tilted in such a direction.

A major consequence of adopting a lower systemic velocity for Puppis A is the change in the kinematic distance. At $v \simeq +16$ km s$^{-1}$, the corresponding distance would be 2.2 kpc according to the Galactic rotation model of Fich, Blitz & Stark (1989). This value has been widely used in the literature. At the new systemic velocity suggested in this paper, $+10.0 \pm 2.5$ km s$^{-1}$, the distance is re-determined as $d = 1.3 \pm 0.3$ kpc, where the quoted uncertainty is based solely on applying the model to the velocity range assumed. An alternative Galactic rotation model proposed by Brand & Blitz (1993) produces a rather different result: $d = 2.0 \pm 0.3$ kpc which, incidentally, is very close to the distance thoroughly used so far. This model has the advantage that all longitudes are covered, while the data set used by Fich et al. (1989) presents a gap from 245° to 351°. However, Brand & Blitz (1993) include three sources approximately describing an ∼1° arc around Puppis A: BBW129, BBW141A, and BBW149, which have very close velocities ($v_{\rm LSR}$ = +9.4, + 10.0, and +8.1) but very discrepant distances: 0.59, 1.85,

and 2.49 kpc respectively. Clearly, the dispersion in distances for such close velocities indicates that strong non-circular motions are taking place in this region of the Galaxy, as remarked by the authors.

As an independent estimate of the distance, we used the model developed by Chen et al. (1999) which associates the colour excess $E(B-V)$ of a certain source with its distance (see e.g. Reynoso et al. 2006). We assume the standard relation between the optical extinction $A_{\rm v}$ and the reddening (e.g. Mathis 1990)

$$E(B-V) = \frac{A_{\rm v}}{3.1} \tag{5}$$

for diffuse dust, and apply the $A_{\rm v} - N_{\rm H}$ relation derived by Güver & Özel (2009) for SNRs:

$$N_{\rm H} = (2.21 \pm 0.09) \times 10^{21} A_{\rm v}, \tag{6}$$

where $N_{\rm H}$ is the hydrogen column density in cm$^{-2}$ based on measurements of X-ray extinction. Gotthelf & Halpern (2009) analysed Newton X-Ray Multi-Mirror Mission observations towards the CCO in Puppis A and found $N_{\rm H} = (4.80 \pm 0.06) \times 10^{21}$ cm$^{-2}$, hence $E(B-V) = 0.70 \pm 0.04$. To apply the reddening-distance model, we estimate the total reddening in the direction of Puppis A produced by the Galactic plane along the line of sight to be $1.58 \pm 0.05$ mag (Schlafly & Finkbeiner 2011). The other two parameters used by the model are the distance of the Sun to the Galactic plane, $z_\odot$, and the scaleheight of the Galactic plane absorbing dust, $h$. Replacing both parameters by $h = 117.7 \pm 4.7$ pc (Kos et al. 2014) and $z_\odot = 19.6 \pm 2.1$ pc (Reed 2006), respectively, the distance to Puppis A turns out to be $d = 1.2 \pm 0.2$ kpc, in excellent agreement with the value obtained through the Galactic rotation model of Fich et al. (1989), which we will adopt hereafter since it contains this latter result as well. A 1 kpc distance had also been derived by Zarnecki et al. (1978) based on the absorption column density of cold gas which yielded the best fit to the continuum X-ray spectrum.

The closer distance would have significant implications in the interpretation of the CCO in Puppis A. Becker et al. (2012) computed its proper motion to be $71 \pm 12$ mas yr$^{-1}$ based on four different measurements over one decade. At a distance of $1.3 \pm 0.3$ kpc, this velocity translates into $440 \pm 175$ km s$^{-1}$. This value is in excellent agreement with the mean pulsar space velocity of $440 \pm 40$ km s$^{-1}$ (Hobbs et al. 2005) and, since it does not exceed 500 km s$^{-1}$, there would be no need to invoke a hydrodynamic recoil mechanism, as proposed by Becker et al. (2012) to explain the anomalously high-velocity kick.

With the distance reduced to 1.3 kpc, the radius of Puppis A would be $\lesssim 10$ pc, and the expansion velocity, $v_{\rm exp} = \frac{2}{5} R/t \simeq 750$ km s$^{-1}$, where the $\frac{2}{5}$ factor applies if the SNR is assumed to be in the Sedov phase. These values for size and expansion velocity, which would be 70 per cent higher with the previous distance of 2.2 kpc, are more in line with typical sizes and velocities of SNRs older than thousand years (Chiad, Ali & Hassani 2015). Overall, although the ~2 kpc distance cannot be completely ruled out, there are plenty of arguments in favour of Puppis A having a distance closer to 1 kpc.

### 4.2 An interstellar bubble created by the progenitor of Puppis A?

As shown in Section 3.2, a shell-like structure is observed in the velocity range from about +6.7 to +10 km s$^{-1}$. From Fig. 8, we can estimate for the shell an angular radius of about 0.°6. In what follows we will discuss if this structure could have been created by the progenitor of Puppis A. In this regard, it is important to note that the structure is observed in a narrow velocity range, less than 5 km s$^{-1}$, implying a low expansion velocity, which is expected if the shell was blown by a star that has ceased its mass ejection activity long ago, after exploding as an SN.

As pointed out by Hwang et al. (2008), the progenitor had a mass between 15 and 25 $M_\odot$, which implies a spectral type between O7 and O9.5 during the main-sequence phase (Martins, Schaerer & Hillier 2005). Taking this range into account, we now analyse whether such a star could have created the observed H I shell. To this end we need to assume a value for the original ambient density, i.e. the density found by the high-mass star during its main-sequence phase. As a rough estimate, we use the Galactic density distribution proposed by Kalberla & Dedes (2008) for Galactocentric distances in the range $7 \leq R_{\rm GC} \leq 35$ kpc, given by

$$n \sim n_{\rm o}\, {\rm e}^{-(R_{\rm GC} - {\rm R}_\odot)/R_{\rm n}} \tag{7}$$

where $n_{\rm o} = 0.9$ cm$^{-3}$, $R_\odot = 8.5$ kpc, and $R_{\rm n} = 3.15$ kpc is a scalelength. Adopting $R_{\rm GC} = 9$ kpc for Puppis A, we obtain $n \sim 0.8$ cm$^{-3}$.

The size achieved for a structure created by the wind energy injected by a given star depends mainly on the wind properties. The mass-loss rates ($\dot{M}$) and terminal wind velocities ($v_{\rm w}$) assumed in this paper for the different possible spectral types are given in Table 2, and were estimated from de Jager, Nieuwenhuijzen & van der Hucht (1988),

$$\log \dot{M} = 1.769 \log \frac{L}{{\rm L}_\odot} - 1.676 \log T_{\rm eff} - 8.158 \tag{8}$$

$$\log v_{\rm w} = 1.23 - 0.3 \log \frac{L}{{\rm L}_\odot} + 0.55 \log \frac{M}{{\rm M}_\odot} + 0.64 \log T_{\rm eff}, \tag{9}$$

where $L$ is the stellar luminosity expressed in solar luminosity units, $M$ is the stellar mass expressed in solar masses, and $T_{\rm eff}$ is the effective stellar temperature in Kelvin. For each spectral type, the basic stellar parameters ($L$, $M$, and $T_{\rm eff}$) were assumed to be the values given by Martins et al. (2005).

The strong impact of the star upon the ISM takes place during the whole main-sequence phase, whose duration depends on the stellar mass. The adopted lifetimes were taken from the tables of Schaller et al. (1992) and are shown in column 4 of Table 2. To estimate the radius reached by the structure at the end of the main-sequence phase, we follow the evolution model of Weaver et al. (1977) which, for the constant wind momentum phase, gives

$$R = 0.83 \left(\frac{\dot{M}\, V_{\rm w}}{\rho_0}\right)^{1/4} t^{1/2}, \tag{10}$$

where $\rho_0$ is the density of the ambient medium assumed uniform. The values obtained are given in the fifth column of Table 2.

As mentioned above, the observed structure has an angular radius of about 0.°6. In the last column of Table 2, the distance needed for the linear radius of the shell to be equal to the radius estimated through equation (10) (column 5 in Table 2) are given. As can be seen, the derived distance is from 1.0 to 1.2 kpc, in excellent agreement with the new estimated distance for Puppis A (see Section 4.1). Thus, in view of these results, it seems completely possible that the star progenitor of Puppis A has created the observed H I bubble.

Finally, we inspected the infrared emission in the area to see whether the observed shell has an IR counterpart. Fig. 9 shows a two colour image of the area. The *Wide-field Infrared Survey Explorer* (*WISE*; Wright et al. 2010) 22 μm emission is shown in green and the AKARI (Takita et al. 2015) 140 μm, in red. From this image, it is clear that the infrared emission related to Puppis

**Table 2.** Stellar parameters.

| Spectral type | Mass-loss rate $\times 10^{-8}$ $M_\odot$ yr$^{-1}$ | Wind velocity (km s$^{-1}$) | Main-sequence lifetime (Myr) | Radius achieved (pc) | Distance[a] (kpc) |
|---|---|---|---|---|---|
| O7 | 1.9 | 2412 | 6.3 | 14.6 | 1.2 |
| O7.5 | 1.4 | 2388 | 7.3 | 14.5 | 1.2 |
| O8 | 1.0 | 2364 | 8.0 | 14.0 | 1.1 |
| O8.5 | 0.7 | 2355 | 8.2 | 12.9 | 1.1 |
| O9 | 0.5 | 2332 | 9.0 | 12.5 | 1.0 |
| O9.5 | 0.4 | 2311 | 10.5 | 12.4 | 1.0 |

[a]Distance necessary to reproduce the linear radii in column 5 for an angular radius of 0.°6.

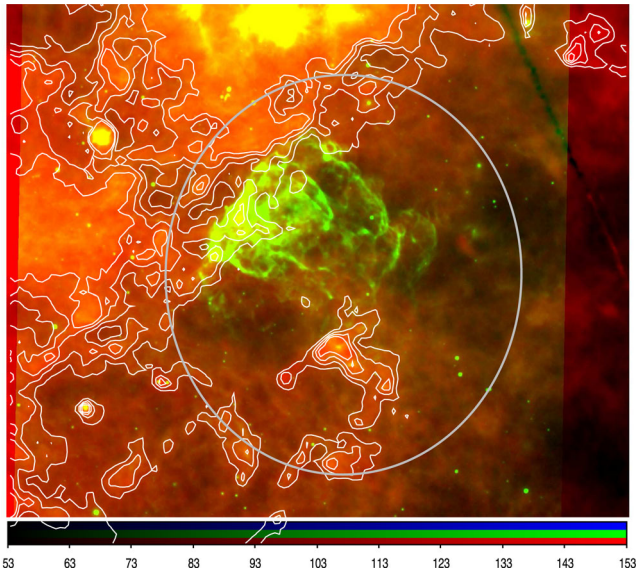


**Figure 9.** Composite image of the region of Puppis A. The image shows *WISE* 22 μm emission in green and the AKARI 140 μm in red and contours, which correspond to the emission at 120, 130, 140, and 150 MJy sr$^{-1}$. The ellipse is the same as Fig. 8 and shows the outline of the suggested H I bubble.

A is higher at 22 μm, while at longer wavelengths, where the IR emission traces cooler dust components, an arc-shaped structure is detected showing a good morphological correlation with the southern part of observed H I bubble (indicated by the ellipse). A striking infrared structure is detected inside the ellipse at about ($\alpha$, $\delta$) = ($8^h21^m45^s$, $-43°18'$) (see Fig. 9). At this location, there is a dark cloud catalogued as DCld 260.6-3.7 by Otrupcek, Hartley & Wang (2000). However, since this source has velocity components at $v$ = +4.5 and +6.4 km s$^{-1}$, it is clearly a foreground cloud not related to Puppis A.

## 5 CONCLUSIONS

We have performed H I observations using the ATCA and subsequently combined these data with single-dish observations, to produce an H I mosaic around the SNR Puppis A. The resultant data have high sensitivity (2–9 mJy beam$^{-1}$), good spatial resolution (118.″3 × 88.″9) and a spectral resolution of 0.82 km s$^{-1}$. We use these data to investigate the physical properties of Puppis A in two ways.

(i) We focus on five unresolved continuum point sources from Reynoso & Walsh (2015) and investigate the H I absorption against the background continuum of these sources. In sources 1, 3, and 5, we find H I absorption at velocities up to $\gtrsim$100 km s$^{-1}$, as well as negative spectral indices confirming their extragalactic origin. In addition to this, we also identify G260.72-3.16, which is found on the eastern edge of the SNR, as a background source, probably extragalactic, approximately 2 arcmin long and oriented north–south. We have filtered out the contribution from these background sources and discuss that the best match for the velocity of the SNR is +10.0 ± 2.5 km s$^{-1}$, which is significantly smaller than found by previous work.

(ii) We investigated the morphology of H I emission over Puppis A and surrounding regions. We find a good match of continuum and H I emission morphologies at velocities of +7.51, +9.98, and +12.46 km s$^{-1}$. This provides further evidence that the systemic velocity of Puppis A is found within this range although a moderate match at higher velocities does not permit to fully rule out the previously accepted velocity of +16 km s$^{-1}$. We also see some evidence for a shell-like structure in the H I emission in the velocity range of +6.69 to +9.98 km s$^{-1}$. This shell structure appears to surround the SNR, seen in radio continuum emission. We interpret this shell as a bubble in the H I emission that was created by the SN explosion.

Based on our alternative systemic velocity of Puppis A of +10.0 ± 2.5 km s$^{-1}$, we compare this velocity to Galactic rotation curves in order to determine a kinematic distance. We therefore revise the estimated distance of Puppis A to 1.3 ± 0.3 kpc. This distance is confirmed by a comparison to the distance separately estimated based on a colour excess model.

Given the revised distance, we calculate a proper motion velocity of 440 ± 175 km s$^{-1}$ for the CCO, which is significantly smaller than previous estimates and does not require a hydrodynamic recoil mechanism to accelerate it to unusually high velocities. We estimate the radius of Puppis A to be ∼10 pc, with an expansion velocity of ∼750 km s$^{-1}$, compatible with an SNR older than 1000 yr.

## ACKNOWLEDGEMENTS

We acknowledge Peter Kalberla for providing us with Parkes H I data from the GASS and fixing calibration problems in its original version. We appreciate useful discussions with Laura Richter, Timothy Shimwell, and Mark Wieringa for solving the mosaic field name length bug, and Jamie Stevens for support to solve the 1 MHz zoom mode bug. This research was partially funded by CONICET grants PIP 114-200801-00428 and 112-201207-00226. The Australia Telescope Compact Array is part of the Australia Telescope National Facility which is funded by the Commonwealth of Australia for operation as a National Facility managed by CSIRO. EMR and SC are members of the Carrera del Investigador Científico of CONICET, Argentina.

## REFERENCES


Becker W., Prinz T., Winkler P. F., Petre R., 2012, ApJ, 755, 141
Brand J., Blitz L., 1993, A&A, 275, 67
Chen B., Figueras F., Torra J., Jordi C., Luri X., Galadí-Enríquez D., 1999, A&A, 352, 459
Chiad B. T., Ali L. T., Hassani A. S., 2015, Int. J. Astron. Astrophys., 5, 125
de Jager C., Nieuwenhuijzen H., van der Hucht K. A., 1988, A&AS, 72, 259
Dickey J. M., McClure-Griffiths N. M., Gaensler B. M., Green A. J., 2003, ApJ, 585, 801
Dubner G. M., Arnal E. M., 1988, A&AS, 75, 363
Fich M., Blitz L., Stark A. A., 1989, ApJ, 342, 272
Frail D. A., Goss W. M., Reynoso E. M., Giacani E. B., Green A. J., Otrupcek R., 1996, AJ, 111, 1651
Gotthelf E. V., Halpern J. P., 2009, ApJ, 695, L35
Güver T., Özel F., 2009, MNRAS, 400, 2050
Hewitt J. W., Grondin M.-H., Lemoine-Goumard M., Reposeur T., Ballet J., Tanaka T., 2012, ApJ, 759, 89
Hobbs G., Lorimer D. R., Lyne A. G., Kramer M., 2005, MNRAS, 360, 974
Hwang U., Flanagan K. A., Petre R., 2005, ApJ, 635, 355
Hwang U., Petre R., Flanagan K. A., 2008, ApJ, 676, 378
Kalberla P. M. W., Dedes L., 2008, A&A, 487, 951
Kos J. et al., 2014, Science, 345, 791
Martins F., Schaerer D., Hillier D. J., 2005, A&A, 436, 1049
Mathis J. S., 1990, ARA&A, 28, 37
McClure-Griffiths N. M. et al., 2009, ApJS, 181, 398
Otrupcek R. E., Hartley M., Wang J.-S., 2000, PASA, 17, 92
Paron S., Dubner G., Reynoso E., Rubio M., 2008, A&A, 480, 439
Petre R., Becker C. M., Winkler P. F., 1996, ApJ, 465, L43
Reed B. C., 2006, J. R. Astron. Soc. Can., 100, 146
Reynoso E. M., Walsh A. J., 2015, MNRAS, 451, 3044
Reynoso E. M., Dubner G. M., Goss W. M., Arnal E. M., 1995, AJ, 110, 318
Reynoso E. M., Green A. J., Johnston S., Dubner G. M., Giacani E. B., Goss W. M., 2003, MNRAS, 345, 671
Reynoso E. M., Dubner G., Giacani E., Johnston S., Green A. J., 2006, A&A, 449, 243
Reynoso E. M., Hughes J. P., Moffett D. A., 2013, AJ, 145, 104
Sault R. J., Teuben P. J., Wright M. C. H., 1995, in Shaw R. A., Payne H. E., Hayes J. J. E., eds, ASP Conf. Ser. Vol. 77, Astronomical Data Analysis Software and Systems IV. Astron. Soc. Pac., San Francisco, p. 433
Schaller G., Schaerer D., Meynet G., Maeder A., 1992, A&AS, 96, 269
Schlafly E. F., Finkbeiner D. P., 2011, ApJ, 737, 103
Takita S. et al., 2015, PASJ, 67, 51
Turner B. E., 1982, ApJ, 255, L33
Weaver R., McCray R., Castor J., Shapiro P., Moore R., 1977, ApJ, 218, 377
Winkler P. F., Petre R., 2007, ApJ, 670, 635
Winkler P. F., Tuttle J. H., Kirshner R. P., Irwin M. J., 1988, in Roger R. S., Landecker T. L., eds, IAU Colloq. 101: Supernova Remnants and the Interstellar Medium. Cambridge Univ. Press, Cambridge, p. 65
Woermann B., Gaylard M. J., Otrupcek R., 2000, MNRAS, 317, 421
Wright E. L. et al., 2010, AJ, 140, 1868
Zarnecki J. C., Culhane J. L., Toor A., Seward F. D., Charles P. A., 1978, ApJ, 219, L17
Zavlin V. E., Trümper J., Pavlov G. G., 1999, ApJ, 525, 959


This paper has been typeset from a TEX/LATEX file prepared by the author.